



High dynamic range 3D shape measurement based on the intensity response function of a camera

LIANG ZHANG,^{1,2,3} QIAN CHEN,^{1,2,4} CHAO ZUO,^{1,2,3,5}  AND SHIJIE FENG^{1,2,3,*}

¹School of Electronic and Optical Engineering, Nanjing University of Science and Technology, No. 200 Xiaolingwei Street, Nanjing, Jiangsu Province 210094, China

²Jiangsu Key Laboratory of Spectral Imaging and Intelligent Sense, Nanjing, Jiangsu Province 210094, China

³Smart Computational Imaging Laboratory (SCILab), Nanjing University of Science and Technology, Nanjing, Jiangsu Province 210094, China

⁴e-mail: chenqian@njust.edu.cn

⁵e-mail: zuochao@njust.edu.cn

*Corresponding author: geniusshijie@163.com

Received 29 September 2017; revised 18 January 2018; accepted 18 January 2018; posted 19 January 2018 (Doc. ID 308245); published 15 February 2018

Fringe projection profilometry has been widely used in many fields for its advantages such as high speed, high accuracy, and robustness to environmental illumination and surface texture. However, it is vulnerable to high dynamic range (HDR) objects. To this end, we propose a technique that can enhance the dynamic range of the fringe projection profilometry system. According to the surface reflectivities of the measured objects, several groups of fringe patterns with optimal light intensities are generated based on the intensity response function of a camera. The HDR fringe images are acquired by fusing these fringe patterns, and a three-step phase-shifting algorithm is used to obtain the unwrapped phase from the fused images. Experimental results demonstrate that the proposed technique can accurately measure objects with an HDR of surface reflectivity variation. © 2018 Optical Society of America

OCIS codes: (120.0120) Instrumentation, measurement, and metrology; (150.6910) Three-dimensional sensing; (120.5050) Phase measurement; (100.2000) Digital image processing.

<https://doi.org/10.1364/AO.57.001378>

1. INTRODUCTION

Fringe projection profilometry is an active optical 3D shape measurement technology based on structured light and stereo matching. It has been applied extensively in many fields [1,2] benefiting from its superiorities of high speed and high accuracy. A fringe projection system generally consists of a camera, a projector, and a computer. A set of designed fringe patterns is projected onto the measured objects. Then the camera captures the corresponding deformed fringe patterns, which contain the phase information of measured objects. The phase information can be extracted by using appropriate phase decoding algorithms [3,4]. Combined with the geometric parameters obtained by calibration in advance, we can calculate the real-world 3D coordinates of measured objects [5,6].

In photography, revealing details in the dark region requires high exposures, while preserving details in the bright region requires low exposures. Most conventional cameras cannot provide this large range of exposure values with a single exposure. As a result, the conventional camera does not perform well when photographing high dynamic range (HDR) objects. To overcome

this problem, Zhang and Yau [7] proposed a technique called HDR scanning. For this multiexposure technique, a sequence of fringe images is taken at different exposure times. To get high-quality fringe patterns, the areas with high reflectivity are extracted from the short exposure images, while the areas with low reflectivity are extracted from the long exposure images. The brightest but not saturated pixels are chosen to integrate into new HDR images. This method improves dynamic range of measurement effectively. However, since the effect of exposure time is not quantified, a large number of images taken at different exposure time are required when measuring complex HDR objects. This method thus has disadvantages of being time-consuming and redundant regarding image data. To overcome these disadvantages, Ekstrand and Zhang [8] proposed a technique that can quantify the effect of exposure time based on the feedback from the reflectivity of measured objects. In this technique, a trade-off must be made between overexposing the brightest areas of objects and losing the fringes in the darkest areas of objects in shadow. This means that it cannot compensate for objects with very wide variation of reflectivity.

Adjusting the light intensity of the projector is another way of solving the HDR problem. Zhang *et al.* [9] proposed a method that can acquire HDR fringe images by controlling the light intensity of projection patterns at pixel level based on the feedback from reflected images. A proper light intensity of a pixel in the projector frame is derived from the camera response function to ensure that the corresponding pixel in the image frame is not saturated. Therefore, this method requires accurate calculation of the homography matrix from the camera to the projector that needs complicated compensation algorithms to reduce matching error. This increases the computation load, and it is difficult to guarantee the measurement accuracy.

In addition, other methods have been proposed to solve the HDR problem by using polarization filters [10], color filters [11], and multiple cameras [12]. However, they all require additional hardware to improve the performance of their systems, possibly leading to increased cost or complex calculations.

In this paper, we propose a technique that can solve the HDR problem of the fringe projection profilometry effectively. The proposed technique can generate fringe patterns with proper light intensities by calculating the reflectance characteristics of measured objects with the intensity response function of a camera that is derived from the reflection model. And an image fusion algorithm is available used for image enhancement. Compared to conventional methods, our method has the following advantages:

- (1) It reduces the number of fringe images and avoids complex calculation, improving the efficiency of measurement.
- (2) It can extract the region of interest from the measured objects, making the measurement more flexible.
- (3) It needs no additional hardware facilities, so it is easy to be applied to other fringe projection profilometry systems.

2. PRINCIPLE

A. Three-Step Phase-Shifting Algorithm

Phase-shifting algorithms are widely used in the 3D shape measurement. In this paper, a three-step phase-shifting algorithm is applied to the phase measurement. The fringe image intensities with a phase shift of $2\pi/3$ are written as

$$I_1(x, y) = I'(x, y) + I''(x, y) \cos \left[\varphi(x, y) - \frac{2\pi}{3} \right], \quad (1)$$

$$I_2(x, y) = I'(x, y) + I''(x, y) \cos[\varphi(x, y)], \quad (2)$$

$$I_3(x, y) = I'(x, y) + I''(x, y) \cos \left[\varphi(x, y) + \frac{2\pi}{3} \right], \quad (3)$$

where (x, y) is the pixel coordinate in the image plane, $I'(x, y)$ is the average intensity, $I''(x, y)$ is the intensity modulation, and $\varphi(x, y)$ is the phase to be measured. Solving Eqs. (1)–(3), we can obtain

$$\varphi(x, y) = \tan^{-1} \frac{\sqrt{3}[I_1(x, y) - I_3(x, y)]}{2I_2(x, y) - I_1(x, y) - I_3(x, y)}. \quad (4)$$

The $\varphi(x, y)$ value ranges from $-\pi$ to $+\pi$ and is also known as the wrapped phase. To obtain a continuous phase map, we need a phase unwrapping algorithm to remove the 2π phase discontinuities. Over the years, numerous phase unwrapping algorithms have been developed. In this paper, we choose the

multifrequency temporal phase unwrapping algorithm [13] to obtain the unwrapped phase.

B. Analysis of Phase Error Caused by Saturation

For an 8-bit grayscale digital camera, its light intensity range is 0~255. For the purpose of simplification, we suppose the intensity error is introduced only from saturation. For N -step phase-shifting, the light intensity value of the image can be described as

$$I_n^C(x, y) = \begin{cases} I_n^C(x, y) & I_n^C(x, y) \leq 255 \\ 255 & I_n^C(x, y) > 255 \end{cases}, \quad (5)$$

where subscript n means the n th image, $I_n^C(x, y)$ is the real light intensity value, and $I_n^C(x, y)$ is the light intensity captured by the camera. The intensity error caused by saturation can be written as

$$\Delta I_n^C(x, y) = \begin{cases} 0 & I_n^C(x, y) \leq 255 \\ I_n^C(x, y) - 255 & I_n^C(x, y) > 255 \end{cases}. \quad (6)$$

According to the phase-shifting algorithm [14], the phase error can be calculated as

$$\Delta\varphi(x, y) = \frac{2}{NI''(x, y)} \sum_{n=0}^{N-1} \sin \left[\varphi(x, y) - \frac{2\pi n}{N} \right] \Delta I_n^C(x, y). \quad (7)$$

It can be seen from Eq. (7) that if N is large enough, the phase error can be negligible. However, projecting too many phase-shift patterns will reduce the efficiency of measurement. So, we solve the saturation problem by eliminating $\Delta I_n^C(x, y)$ instead of increasing N .

C. Derivation of the Intensity Response Function

To explore the relationship between the light intensity captured by camera and that outputted from the projector, we should analyze the influence of different illumination sources first. Typically, in a fringe projection system, the following illumination sources need to be considered: (1) the ambient light coming directly to the camera sensor with an intensity of I^A , (2) the projected light with an intensity of I^P reflected by the measured object with surface reflectivity of ρ , ρI^P , and (3) the ambient light with an intensity of I^O reflected by the object, ρI^O . The schematic diagram is illustrated in Fig. 1.

Assuming the camera sensitivity is γ , the exposure time is t , and the noise of the sensor is I^N , the intensity I^C captured by the camera can then be described as

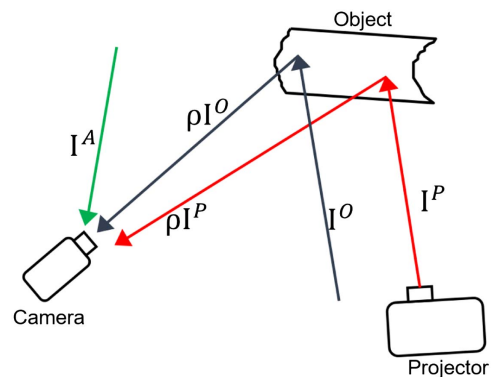


Fig. 1. Different sources of illumination.

$$I^C(x, y) = \gamma t [\rho(x, y) I^P(u, v) + \rho(x, y) I^O + I^A] + I^N, \quad (8)$$

where (u, v) denotes the pixel coordinate in the projector plane. Letting

$$a(x, y) = \gamma t \rho(x, y), \quad (9)$$

$$b(x, y) = \gamma t [\rho(x, y) I^O + I^A] + I^N. \quad (10)$$

Equation (8) can be simplified as

$$I^C(x, y) = a(x, y) I^P(u, v) + b(x, y). \quad (11)$$

For a given measured object and measurement environment, if the camera sensitivity γ and the exposure time t remain constant, $I^C(x, y)$ depends only on $I^P(u, v)$. Equation (11) is the so-called intensity response function. To solve $a(x, y)$ and $b(x, y)$, we first have to know the value of $I^P(u, v)$ and $I^C(x, y)$. $I^C(x, y)$ can be obtained easily from the image, while $I^P(u, v)$ depends on the pixel coordinate (u, v) . For each pixel (x, y) of the camera, we can get the initial corresponding pixel (u, v) of the projector by homography matrix. However, the process of solving the homography matrix is complicated. And it is difficult to ensure the accuracy and reliability of the homography matrix. Therefore, we project a set of uniform patterns with different light intensities onto the measured object to avoid calculating the homography matrix. For an 8-bit projector, the uniform patterns are expressed as

$$\begin{cases} I_i^P = (i - 1) \times s \\ 0 \leq I_i^P \leq 255 \\ i = 1, 2, \dots, T \end{cases}, \quad (12)$$

where i is the i th pattern, s is the step size, and T is the total number of the uniform patterns. Because the image pixels behave nonlinearly when saturated, I_i^P should be selected reasonably to avoid image saturation (255 for an 8-bit camera). Then Eq. (11) can be rewritten as

$$\begin{cases} I_i^C(x, y) = a(x, y) I_i^P + b(x, y) \\ 0 \leq I_i^C(x, y) < 255 \end{cases}. \quad (13)$$

Theoretically, two patterns are sufficient to solve $a(x, y)$ and $b(x, y)$. In consideration of noise, more patterns should be used to increase the accuracy. For different measured objects, we can get enough uniform patterns through setting the values of s and T . Equation (13) can be concisely expressed in matrix form as

$$\begin{bmatrix} I_1^P & 1 \\ I_2^P & 1 \\ \vdots & \vdots \\ I_T^P & 1 \end{bmatrix} \cdot \begin{bmatrix} a(x, y) \\ b(x, y) \end{bmatrix} = \begin{bmatrix} I_1^C(x, y) \\ I_2^C(x, y) \\ \vdots \\ I_T^C(x, y) \end{bmatrix}. \quad (14)$$

Assuming the reflection intensity and the ambient light on the object surface do not change during measurement, we can get the values of $a(x, y)$ and $b(x, y)$ by the least squares method.

Figure 2 gives an example of a checkerboard. For the checkerboard, s and T are set to be 20 and 8, respectively. Figure 3 shows the result; it can be seen the $a(x, y)$ of the white square is much greater than the $a(x, y)$ of the black square. So, for the white square, the projected light intensity should be low

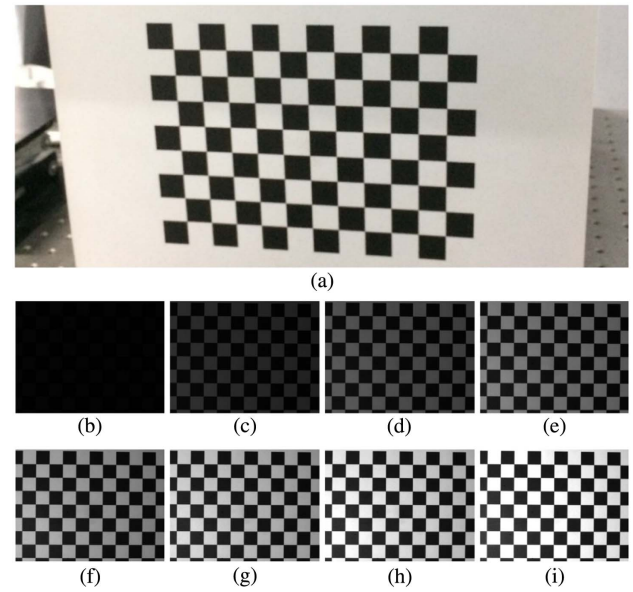


Fig. 2. (a) Photograph of the checkerboard, (b) checkerboard with intensity of 0, (c) checkerboard with intensity of 20, (d) checkerboard with intensity of 40, (e) checkerboard with intensity of 60, (f) checkerboard with intensity of 80, (g) checkerboard with intensity of 100, (h) checkerboard with intensity of 120, and (i) checkerboard with intensity of 140.

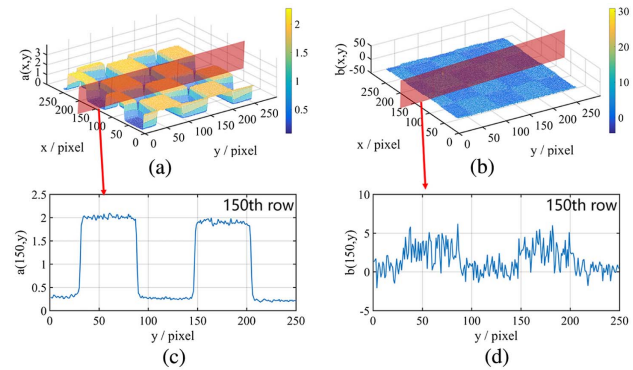


Fig. 3. (a) $a(x, y)$ of the checkerboard, (b) $b(x, y)$ of the checkerboard, (c) cross-section plot of $a(x, y)$, and (d) cross section plot of $b(x, y)$.

to avoid saturation. For the black square, the projected light intensity should be high to improve the signal-to-noise ratio.

D. Generate Projection Patterns

Theoretically, the optimal intensity I_{opt}^C captured by camera avoids saturation and has a high signal-to-noise ratio. Thus, I_{opt}^C should be 254 for an 8-bit camera. And the corresponding optimal projected light intensity I_{opt}^P can be derived from the intensity response function

$$I_{\text{opt}}^P(x, y) = \frac{I_{\text{opt}}^C(x, y) - b(x, y)}{a(x, y)} = \frac{254 - b(x, y)}{a(x, y)}. \quad (15)$$

Taking into account the fitting error and measurement noise, we have to reserve some gray level space to avoid

saturation. If the reserved value is not large enough, it will cause image saturation in some extreme cases, while if the reserved value is too large, it will reduce the signal-to-noise ratio. For the reserved value, 9 can meet the needs of most experiments. Equation (15) is rewritten as

$$I_{opt}^p(x, y) = \frac{254 - 9 - b(x, y)}{a(x, y)} = \frac{245 - b(x, y)}{a(x, y)}. \quad (16)$$

Equation (16) shows that each pixel (x, y) will correspond to a $I_{opt}^p(x, y)$. However, it is impossible to measure an object with every acquired $I_{opt}^p(x, y)$. Only several projected light intensities would be adequate for general measured objects due to the fact that a single projected light intensity can provide enough intensity for a surface with an appropriate variation range of reflectivity. In the proposed method, the projected light intensities depend on the distribution of $a(x, y)$. $a(x, y)$ is divided into several intervals, and each interval has a corresponding projected light intensity. Therefore, the size of the interval length has a direct impact on the measurement result. The smaller the intervals, the more light intensities will be used. This improves the measurement accuracy but sacrifices the measurement efficiency. In other words, a trade-off must be made between measurement accuracy and efficiency. Many of our experiments have shown that the requirements on both accuracy and efficiency can be satisfied, when the interval length is set to be 1. For a given pixel (x, y) , we can get

$$a(x, y) \in (\text{Floor}(a(x, y)), \text{Floor}(a(x, y) + 1)], \quad (17)$$

where $\text{Floor}()$ is the integral function that takes a real number x and gives the greatest integer that $\text{Floor}(x)$ is less than or equal to x . The serial number k of the interval is

$$k = \text{Floor}(a(x, y)) + 1. \quad (18)$$

The corresponding projected light intensity I_k^p can be expressed as

$$I_k^p = \frac{245 - b_{ul}}{m}, \quad (19)$$

$$\begin{cases} m = a_{ul} & \text{if } a(x, y) \in (\text{Floor}(a_{ul}), \text{Floor}(a_{ul}) + 1] \\ m = k & \text{otherwise} \end{cases}, \quad (20)$$

where a_{ul} is the upper limit value of $a(x, y)$, and b_{ul} is the upper limit of $b(x, y)$. Ideally, a_{ul} is the maximum value of all $a(x, y)$, and b_{ul} is the maximum value of all $b(x, y)$. However, for a digital camera, there are some hot pixels that look much brighter than they should. After eliminating hot pixels, we can get a_{ul} and b_{ul} by statistical analysis. Then, for the use of a three-step phase-shifting algorithm, the average intensity I' of fringe patterns is given by

$$I'(u, v) = \frac{I_k^p}{2}, \quad (21)$$

and the intensity modulation I'' is given by

$$I''(u, v) = \frac{I_k^p}{2}. \quad (22)$$

For the checkerboard shown in Fig. 2(a), its histograms of $a(x, y)$ and $b(x, y)$ are shown in Fig. 4. For the white squares, their $a(x, y)$ is concentrated in interval $[1.3, 2.3]$, while $a(x, y)$ of the black squares is concentrated in interval $[0, 0.6]$.

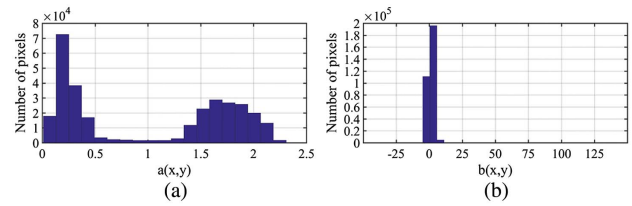


Fig. 4. (a) Histogram of $a(x, y)$ and (b) histogram of $b(x, y)$.

In this case, $a(x, y)$ is divided into two intervals: $[0, 1]$ and $[1, 2.3]$. From Eqs. (18)–(20), we can get the projected light intensities, as follows:

$$I_1^p = \frac{245 - 10}{1} = 235, \quad (23)$$

$$I_2^p = \frac{245 - 10}{a_{ul}} = \frac{245 - 10}{2.3} = 102. \quad (24)$$

From Eqs. (23) and (24), two groups of fringe patterns are generated as follows:

$$\text{Group 1: } \begin{cases} I_{11}^p(u, v) = 117.5 + 117.5 \cos \left[\varphi(u, v) - \frac{2\pi}{3} \right] \\ I_{12}^p(u, v) = 117.5 + 117.5 \cos[\varphi(u, v)] \\ I_{13}^p(u, v) = 117.5 + 117.5 \cos \left[\varphi(u, v) + \frac{2\pi}{3} \right] \end{cases}, \quad (25)$$

$$\text{Group 2: } \begin{cases} I_{21}^p(u, v) = 51 + 51 \cos \left[\varphi(u, v) - \frac{2\pi}{3} \right] \\ I_{22}^p(u, v) = 51 + 51 \cos[\varphi(u, v)] \\ I_{23}^p(u, v) = 51 + 51 \cos \left[\varphi(u, v) + \frac{2\pi}{3} \right] \end{cases}. \quad (26)$$

Figure 5(a) shows a mix material composed of three components: a metal plate made of aluminum, a brown carton, and a black carton. Figure 5(b) shows its histogram of $a(x, y)$. It can be seen that its variation range of $a(x, y)$ is larger than the checkerboard.

For the mix material, its a_{ul} and b_{ul} are 2.5 and 20, respectively. To achieve high measurement accuracy of the mix material, $a(x, y)$ is divided into three intervals: $(0, 1]$, $(1, 2]$, and $(2, 2.5]$. The corresponding projected light intensities are

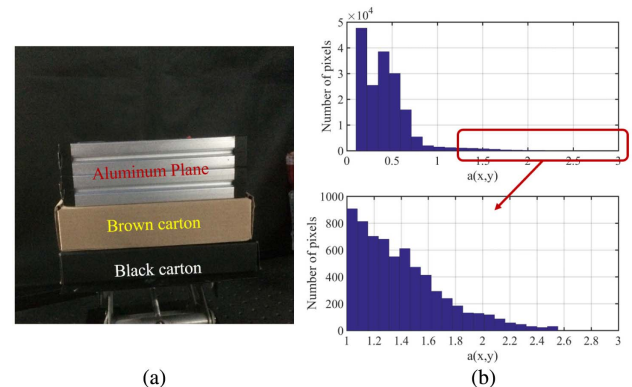


Fig. 5. (a) Photograph of the mix material and (b) histogram of $a(x, y)$.

$$I_1^P = \frac{245 - 20}{1} = 225, \quad (27)$$

$$I_2^P = \frac{245 - 20}{2} = 112, \quad (28)$$

$$I_3^P = \frac{245 - 20}{a_{ul}} = \frac{245 - 20}{2.5} = 90, \quad (29)$$

and we have three groups of fringe patterns as follows:

$$\text{Group 1: } \begin{cases} I_{11}^P(u, v) = 112.5 + 112.5 \cos \left[\varphi(u, v) - \frac{2\pi}{3} \right] \\ I_{12}^P(u, v) = 112.5 + 112.5 \cos[\varphi(u, v)] \\ I_{13}^P(u, v) = 112.5 + 112.5 \cos \left[\varphi(u, v) + \frac{2\pi}{3} \right] \end{cases}, \quad (30)$$

$$\text{Group 2: } \begin{cases} I_{21}^P(u, v) = 56 + 56 \cos \left[\varphi(u, v) - \frac{2\pi}{3} \right] \\ I_{22}^P(u, v) = 56 + 56 \cos[\varphi(u, v)] \\ I_{23}^P(u, v) = 56 + 56 \cos \left[\varphi(u, v) + \frac{2\pi}{3} \right] \end{cases}, \quad (31)$$

$$\text{Group 3: } \begin{cases} I_{31}^P(u, v) = 45 + 45 \cos \left[\varphi(u, v) - \frac{2\pi}{3} \right] \\ I_{32}^P(u, v) = 45 + 45 \cos[\varphi(u, v)] \\ I_{33}^P(u, v) = 45 + 45 \cos \left[\varphi(u, v) + \frac{2\pi}{3} \right] \end{cases}. \quad (32)$$

E. Image Fusion

In actual measurements, fringe images with a high projected light intensity can preserve the detail in the dark region, but they are more likely to cause saturation, while fringe images with a low projected light intensity have a low signal-to-noise ratio in the dark region. Through image fusion, we can combine the merit or the complementarity of the images with different light intensities and obtain new images with more abundant information. As mentioned in the preceding section, we get several groups of fringe patterns with different light intensities. The light intensities of the images captured by the camera are denoted as

$$\begin{cases} I_{k1}^C(x, y) = a(x, y)I_{k1}^P(u, v) + b(x, y) \\ I_{k2}^C(x, y) = a(x, y)I_{k2}^P(u, v) + b(x, y) \\ I_{k3}^C(x, y) = a(x, y)I_{k3}^P(u, v) + b(x, y) \end{cases}, \quad (33)$$

$$k = 1, 2, \dots, [\text{Floor}(a_{ul}) + 1]$$

where k is the serial number of the intervals. The fused images $I_{F1}-I_{F3}$ are formed as the cases

if $a(x, y) > a_{ul}$ or $b(x, y) > b_{ul}$,

$$\begin{cases} I_{F1}(x, y) = 0 \\ I_{F2}(x, y) = 0, \\ I_{F3}(x, y) = 0 \end{cases}, \quad (34)$$

if $a(x, y) \leq a_{ul}$,

$$\begin{cases} I_{F1}(x, y) = 0 \\ I_{F2}(x, y) = 0, \\ I_{F3}(x, y) = 0 \end{cases}, \quad (35)$$

if $a_{ll} < a(x, y) \leq a_{ul}$,

$$\begin{cases} I_{F1}(x, y) = F \cdot \frac{I_{k1}^C(x, y) - b(x, y)}{a(x, y)} \\ I_{F2}(x, y) = F \cdot \frac{I_{k2}^C(x, y) - b(x, y)}{a(x, y)}, \\ I_{F3}(x, y) = F \cdot \frac{I_{k3}^C(x, y) - b(x, y)}{a(x, y)} \end{cases}, \quad (36)$$

$$F = \frac{m}{a_{ul}}, \quad (37)$$

where m can be calculated by Eq. (20), F is a parameter used to ensure the light intensity continuity of the fused images, and a_{ll} is the lower limit value of $a(x, y)$. On an image captured by camera, there are normally noise and shadows, which leads to some invalid points. Invalid points normally have very low light intensities. a_{ll} is used for distinguishing between invalid points and measured objects.

Traditional methods use the intensity modulation $I''(x, y)$ to distinguish invalid points, which cannot perform well when measuring objects with low reflectivity. Figure 6(a) shows a plastic statue and a lifting table. Because of the black color, the captured intensity of the lifting table is very low, meaning the lifting table is hard to distinguish from invalid points when projecting patterns with low light intensities, as shown in Figs. 7(a) and 7(c). In fact, the light intensity of the invalid point hardly changes with the projected light intensity. Therefore, we can distinguish between invalid points and measured objects by

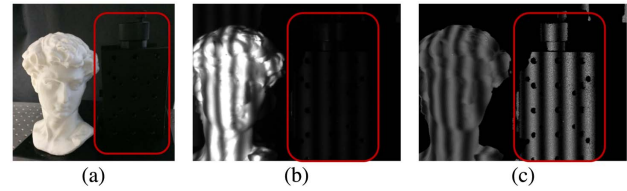


Fig. 6. (a) Photograph of the plastic statue and the lifting table, (b) fringe pattern captured by camera, and (c) fused image.

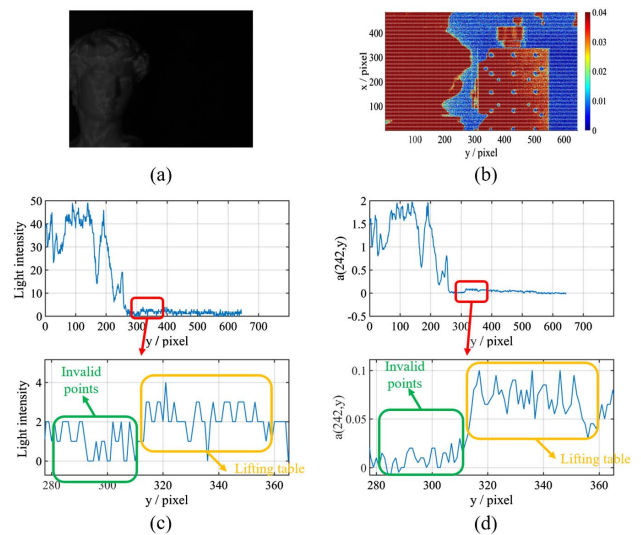


Fig. 7. (a) Image of the plastic statue and the lifting table with intensity of 20, (b) $a(x, y)$ of the plastic statue and the lifting table, (c) cross-section plot of (a), (d) cross-section plot of (b).

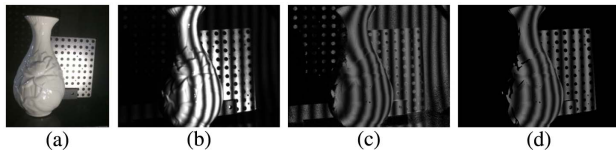


Fig. 8. (a) Photograph of a porcelain vase and an aluminum sheet, (b) fringe pattern captured by camera, (c) fused image ($a_{II} = 0.04$), and (d) fused image ($a_{II} = 0.2$).

analyzing $a(x, y)$. Figures 7(b) and 7(d) show that $a(x, y)$ of the invalid points is less than 0.04, meaning a_{II} of the plastic statue and the lifting table should be set to be 0.04. From Eqs. (34)–(36), we can get the fused image shown in Fig. 6(c). Compared to the original image shown in Fig. 6(b), the fused image has a higher dynamic range, and the light intensity of the lifting table is enhanced.

Experimentally, we can remove almost all invalid points when a_{II} is set to be 0.04. However, it may also enhance unrelated objects, as shown in Fig. 8(c). Therefore a_{II} should be set properly according to the reflectivity of measured objects. For measured objects with high reflectivity, we can increase the value of a_{II} to get a better fused image shown in Fig. 8(d). Thus, a_{II} is not limited to distinguish between invalid points and measured objects. Cooperating with a_{ul} , a_{II} can be used to extract the region of interest from the measurement scene.

3. EXPERIMENTS

To verify the performance of our method, we built a fringe projection system comprising a digital light processing (DLP) projector (model: TI Light Crafter 4500) and an industrial camera (model: AVT GigE Mako G030B). A photograph of the experiment system is shown in Fig. 9. The camera has a resolution of 644×484 at a frame rate of up to 200 fps. The DLP projector has a resolution of 912×1140 at a frame rate of up to 100 fps when projecting 8-bit gray-scale images.

The flowchart of the experiment is shown in Fig. 10. It mainly includes three steps:

Step1: preparation work before the measurement. It includes obtaining the calibration parameters of the system, setting the threshold of the geometry constraint, and generating fringe patterns.

Step2: image generation. In this step, the intensity response function of the camera and image fusion are used to generate HDR fringe images.

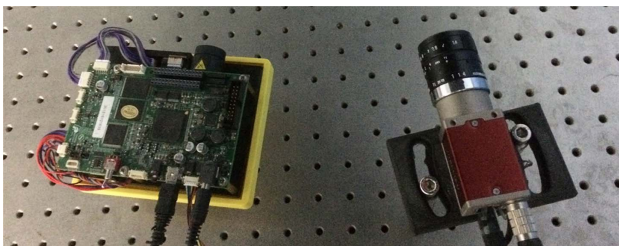


Fig. 9. System setup.

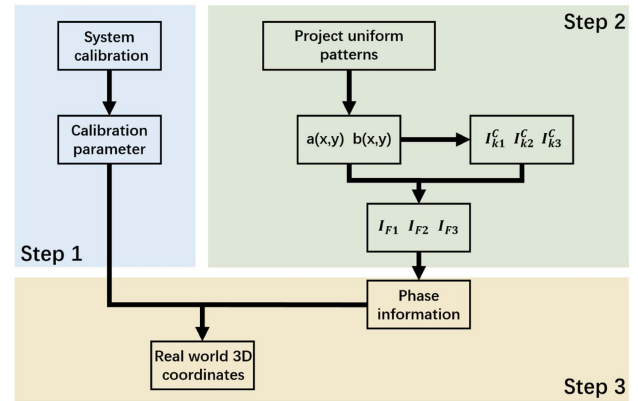


Fig. 10. Flowchart of the proposed technique.

Step3: acquisition of 3D topography of objects. In this step, we adopt the method discussed by Liu [15] to convert the absolute phase to real-world 3D coordinates with MATLAB.

It should be noted that on the basis of experiments and references, the impact of gamma nonlinearity of the Light Crafter 4500 can be neglected. For a commercial projector, it is sensitive to the nonlinear gamma. The gamma deforms the ideal sinusoidal fringe patterns to be nonsinusoidal and introduces error. If the fringe projection system consists of a



Fig. 11. (a) Photograph of the plaster and (b) photograph of the metal wrench.

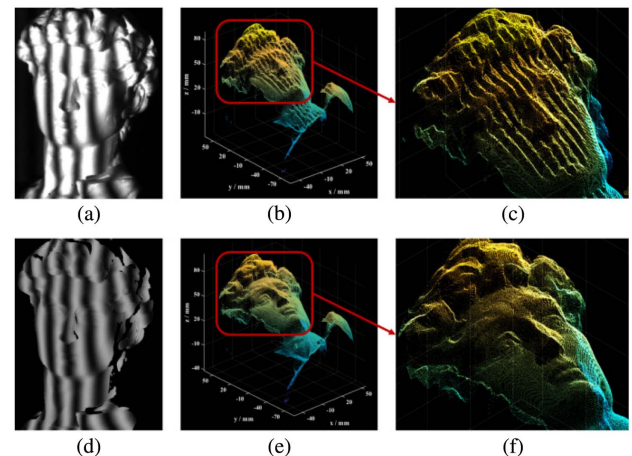


Fig. 12. (a) Representative fringe image with the maximum light intensity of 255, (b) corresponding 3D measurement result of (a), (c) enlarged detail of the region in (b), (d) fused fringe image, (e) corresponding 3D measurement result of (d), (f) enlarged detail of the region in (e).

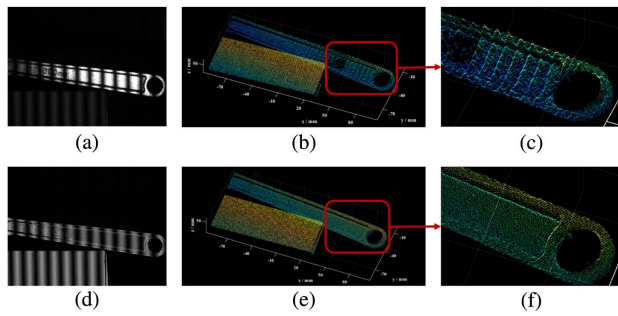


Fig. 13. (a) Representative fringe image with the maximum light intensity of 255, (b) corresponding 3D measurement result of (a), (c) enlarged detail of the region in (b), (d) fused fringe image, (e) corresponding 3D measurement result of (d), (f) enlarged detail of the region in (e).

commercial projector, gamma correction [16] is necessary before taking a measurement.

A. Qualitative Evaluation

To verify our method can produce good 3D measurement results, we measured a plaster cast of David, as shown in Fig. 11(a).

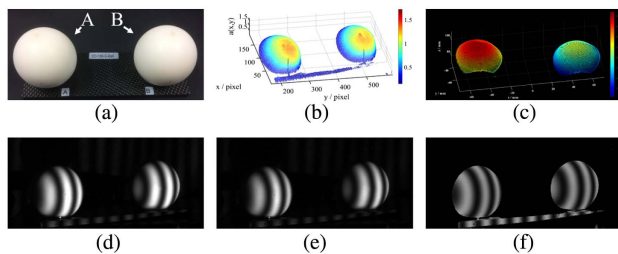


Fig. 14. (a) Photograph of the pair of standard ceramic spheres, (b) $a(x, y)$ of the pair of standard ceramic spheres, (c) corresponding 3D measurement result of (a), (d) representative original fringe image, (e) representative fringe image of Zhang's method, (f) representative fringe image of our method.

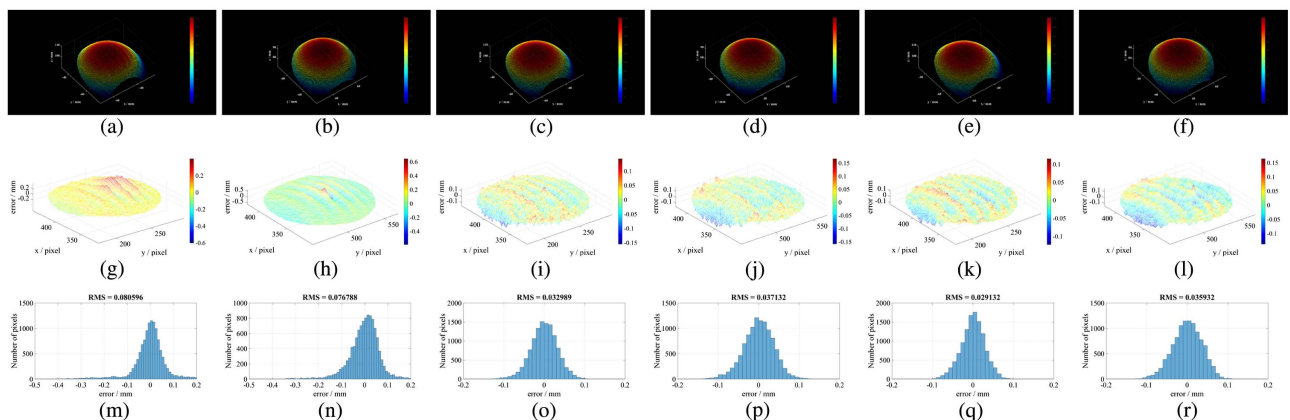


Fig. 15. (a) Original 3D measurement results of the sphere *A*, (b) original 3D measurement results of the sphere *B*, (c) 3D measurement results of the sphere *A* with Zhang's method, (d) 3D measurement results of the sphere *B* with Zhang's method, (e) 3D measurement results of the sphere *A* with our method, (f) 3D measurement results of the sphere *B* with our method, (g) distribution of the errors of (a), (h) distribution of the errors of (b), (i) distribution of the errors of (c), (j) distribution of the errors of (d), (k) distribution of the errors of (e), (l) distribution of the errors of (f), (m) histogram of (g), (n) histogram of (h), (o) histogram of (i), (p) histogram of (j), (q) histogram of (k), (r) histogram of (l).

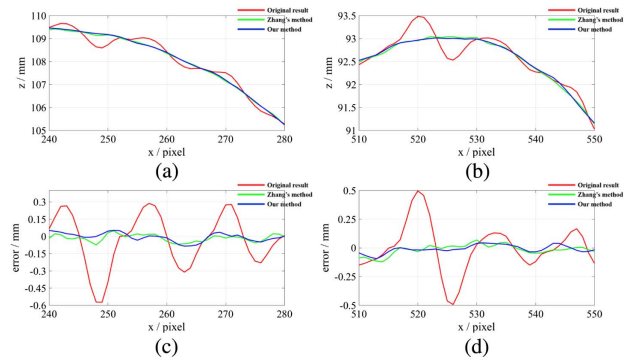


Fig. 16. (a) Cross-section plot of 3D measurement results of the sphere *A*, (b) cross-section plot of 3D measurement results of the sphere *B*, (c) cross-section plot of the measured error of the sphere *A*, (d) cross-section plot of the measured error of the sphere *B*.

The three-step phase-shifting algorithm was used to calculate 3D data. Figure 12(a) shows a representative fringe image with the maximum light intensity of 255, demonstrating large areas of highlight on the plaster. This leads to incorrect measurement areas shown in Figs. 12(b) and 12(c). Figure 12(d) shows a representative fused fringe image obtained by our method, and its corresponding measurement result is shown in Figs. 12(e) and 12(f). Compared to the measurement result in Figs. 12(b) and 12(c), our method can provide more facial details of the plaster.

To further verify the presented method, we tested it on a metal wrench, shown in Fig. 11(b). Its variation range of $a(x, y)$ is larger than that of the plaster because of the metallic specular reflection. Figure 13(a) shows that the saturated regions of specular reflection completely block the fringe patterns, leading to a very poor 3D measurement result shown in Figs. 13(b) and 13(c). By comparison, the measurement result of our method shown in Figs. 13(e) and 13(f) is of high quality.

Table 1. Accuracy Results of the Proposed Method

Method	Identifier	Average Error/mm	RMS/mm
Original	Sphere <i>A</i>	0.048685	0.080596
	Sphere <i>B</i>	0.049234	0.076788
Zhang's method	Sphere <i>A</i>	0.027167	0.032989
	Sphere <i>B</i>	0.031009	0.037132
Our method	Sphere <i>A</i>	0.024033	0.029132
	Sphere <i>B</i>	0.029593	0.035932

The above experiments have demonstrated that the proposed method can provide high-quality 3D measurement results.

B. Quantitative Evaluation

To evaluate our method quantitatively, we measured a pair of standard ceramic spheres. Figure 14(a) shows the pair of standard ceramic spheres of radius 25.4 mm. Its $a(x, y)$ is shown in Fig. 14(b). The result of statistical analysis indicates that its a_{ul} and a_{ll} are 1.6 and 0.15, respectively. So, two projected light intensities are enough to measure the standard ceramic spheres well. The measurement result is shown in Fig. 14(c).

To better describe the accuracy and efficiency of our method, we adopted Zhang's method [7] for comparison. The corresponding fringe images captured by the camera are

shown in Figs. 14(d)–14(f). The measurement results of the sphere *A* and the sphere *B* are displayed separately in Figs. 15(a)–15(f). Figures 16(a) and 16(b), respectively, show one cross-section of the measurement result of the sphere *A* and *B*. From the original result, we can see that there are notable errors because of the saturated pixels, while Zhang's method and our method can obtain high-quality 3D measurement results.

To obtain the measured errors, we used the measured data shown in Figs. 15(a)–15(f) to fit the sphere, and then the fitted spheres were set as the ground truth. The differences between the measured data and the fitted data are shown in Figs. 15(j)–15(l). Figures 15(m)–15(r) show the quantitative histograms of Figs. 15(j)–15(l). Figures 16(c) and 16(d) compare the error of the sphere *A* and the sphere *B* measured with different methods. And the concrete numerical value is shown in Table 1. We can find from Table 1 that the accuracy of our method is slightly higher than Zhang's method.

Moreover, we measured a mix material composed of a porcelain vase and an aluminum sheet shown in Fig. 17(a). From Fig. 17(b), it can be easily found that the mix material has a very wide variation range of $a(x, y)$. Its a_{ul} and a_{ll} are 3.2 and 0.2, respectively. According to Eqs. (18)–(20), the projected light intensities $I_1^p - I_4^p$ are 220, 110, 73, and 68, respectively. I_3^p corresponds closely to I_4^p , so I_1^p , I_2^p , and I_4^p are enough to measure the mix material well. The measurement result is shown in Fig. 17(c).

The representative fringe images of different methods are shown in Figs. 17(d)–17(f). Figures 18(a)–18(c) and 18(g)–18(i) show the measurement results of the porcelain vase. Figures 18(d)–18(f) and 18(j)–18(l) show the measurement results of the aluminum sheet. Because the mix material has no unified standard, we just compared the 3D measurement results, shown in Figs. 19(a) and 19(b).

The above experiments have demonstrated that our method can get highly accurate 3D measurement results. Although Zhang's method can also get highly accurate 3D measurement results, to obtain high-quality fringe images, a large number of exposures are required. For example, we used 11 exposures to measure the pair of standard ceramic spheres, and 20 exposures for the porcelain vase and the aluminum sheet. In other words, Zhang's method needs 11 and 20 groups of fringe images to get highly accurate 3D measurement results. Compared to Zhang's

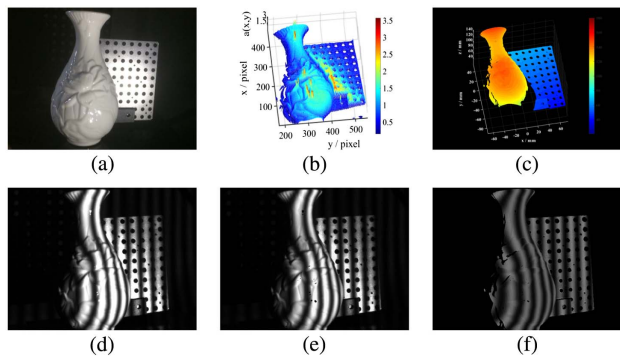


Fig. 17. (a) Photograph of the mix material, (b) $a(x, y)$ of the mix material, (c) 3D measurement result of (a), (d) representative original fringe image, (e) representative fringe image of Zhang's method, (f) representative fringe image of our method.

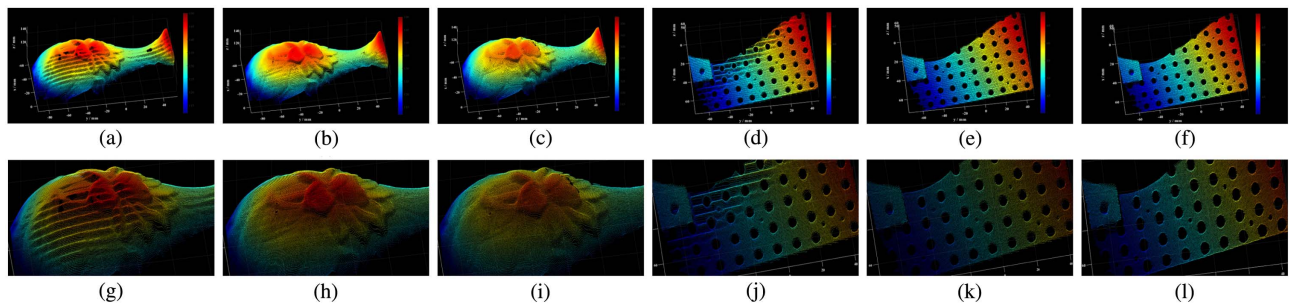


Fig. 18. (a) Original 3D measurement results of the porcelain vase, (b) 3D measurement results of the porcelain vase with Zhang's method, (c) 3D measurement results of the porcelain vase with our method, (d) original 3D measurement results of the aluminum sheet, (e) 3D measurement results of the aluminum sheet with Zhang's method, (f) 3D measurement results of the aluminum sheet with our method, (g) enlarged detail of (a), (h) enlarged detail of (b), (i) enlarged detail of (c), (j) enlarged detail of (d), (k) enlarged detail of (e), (l) enlarged detail of (f).

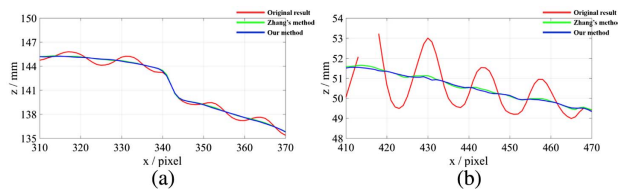


Fig. 19. (a) Cross-section plot of 3D measurement results of the porcelain vase, (b) cross-section plot of 3D measurement results of the aluminum sheet.

method, our method is more efficient. On the one hand, our method can measure objects with fewer groups of fringe images. On the other hand, it also avoids complex formation of each fringe image pixel from a sequence of fringe images with different exposures.

4. CONCLUSIONS

In this paper, we have developed a technique to enhance the dynamic range of a fringe projection system. For measured objects with different reflectance, we use the intensity response function of the camera and image fusion technology to derive HDR fringe images. Compared to conventional methods, the proposed method reduces the number of fringe patterns and avoids the complex matrix calculation. Furthermore, the proposed method can be applied to any existing fringe projection system without any increase in hardware costs.

Funding. Final Assembly “13th Five-Year Plan” Advanced Research Project of China (30102070102); Outstanding Youth Foundation of Jiangsu Province of China (BK20170034); National Defense Science and Technology Foundation of China (0106173); “Six Talent Peaks” project of Jiangsu Province, China (2015-DZXX-009); “333 Engineering” Research Project of Jiangsu Province, China (BRA2016407); Fundamental Research Funds for the Central Universities (30916011322, 30917011204); Open Research Fund in 2017 of Jiangsu Key Laboratory of Spectral Imaging & Intelligent Sense (3091601410414); National Key Technologies R&D Program of China (2017YFF0106403); National Natural Science Foundation of China (NSFC)

(111574152, 61505081, 61705105); China Postdoctoral Science Foundation (2017M621747); Jiangsu Planned Projects for Postdoctoral Research Funds (1701038A).

REFERENCES

1. F. Chen and G. M. Brown, “Overview of 3-D shape measurement using optical methods,” *Opt. Eng.* **39**, 10–22 (2000).
2. F. Blais, “Review of 20 years of range sensor development,” *Proc. SPIE* **13**, 228–240 (2004).
3. R. M. Goldstein, H. A. Zebker, and C. L. Werner, “Satellite radar interferometry: two-dimensional phase unwrapping,” *Radio Sci.* **23**, 713–720 (1988).
4. J. M. Huntley and H. Saldner, “Temporal phase-unwrapping algorithm for automated interferogram analysis,” *Appl. Opt.* **32**, 3047–3052 (1993).
5. R. Legardasáenz, T. Bothe, and W. P. O. Jüptner, “Accurate procedure for the calibration of a structured light system,” *Opt. Eng.* **43**, 464–471 (2004).
6. S. Zhang and P. S. Huang, “Novel method for structured light system calibration,” *Opt. Eng.* **45**, 083601 (2006).
7. S. Zhang and S. T. Yau, “High dynamic range scanning technique,” *Opt. Eng.* **48**, 033604 (2009).
8. L. Ekstrand and S. Zhang, “Autoexposure for three-dimensional shape measurement using a digital-light-processing projector,” *Opt. Eng.* **50**, 123603 (2011).
9. C. Zhang, J. Xu, N. Xi, J. Zhao, and Q. Shi, “A robust surface coding method for optically challenging objects using structured light,” *IEEE Trans. Autom. Sci. Eng.* **11**, 775–788 (2014).
10. S. Feng, Y. Zhang, Q. Chen, C. Zuo, R. Li, and G. Shen, “General solution for high dynamic range three-dimensional shape measurement using the fringe projection technique,” *Opt. Lasers Eng.* **59**, 56–71 (2014).
11. Q. Hu and K. G. Harding, “Shiny parts measurement using color separation,” *Proc. SPIE* **6000**, 60000D (2005).
12. S. Feng, Q. Chen, C. Zuo, and A. Asundi, “Fast three-dimensional measurements for dynamic scenes with shiny surfaces,” *Opt. Commun.* **382**, 18–27 (2017).
13. C. Zuo, L. Huang, M. Zhang, Q. Chen, and A. Asundi, “Temporal phase unwrapping algorithms for fringe projection profilometry: a comparative review,” *Opt. Lasers Eng.* **85**, 84–103 (2016).
14. W. Li and X. Su, “Phase unwrapping algorithm based on phase fitting reliability in structured light projection,” *Opt. Eng.* **41**, 1365–1372 (2002).
15. K. Liu, “Real-time 3-D reconstruction by means of structured light illumination,” Ph.D. dissertation (University of Kentucky, 2010).
16. D. L. Lau, K. Liu, L. G. Hassebrook, Q. Hao, and Y. Wang, “Gamma model and its analysis for phase measuring profilometry,” *J. Opt. Soc. Am. A* **27**, 553–562 (2010).